Article

Nanocrystalline CaWO$_4$ and ZnWO$_4$ Tungstates for Hybrid Organic–Inorganic X-ray Detectors

Inga Pudza [1,*], Kaspars Pudzs [1], Andrejs Tokmakovs [1], Normunds Ralfs Strautnieks [1], Aleksandr Kalinko [1,2] and Alexei Kuzmin [1]

1   Institute of Solid State Physics, University of Latvia, Kengaraga Street 8, LV-1063 Riga, Latvia
2   Deutsches Elektronen-Synchrotron DESY, Notkestrasse 85, D-22607 Hamburg, Germany
*   Correspondence: inga.pudza@cfi.lu.lv

Abstract: Hybrid materials combining an organic matrix and high-Z nanomaterials show potential for applications in radiation detection, allowing unprecedented device architectures and functionality. Herein, novel hybrid organic–inorganic systems were produced using a mixture of tungstate (CaWO$_4$ or ZnWO$_4$) nanoparticles with a P3HT:PCBM blend. The nano-tungstates with a crystallite size of 43 nm for CaWO$_4$ and 30 nm for ZnWO$_4$ were synthesized by the hydrothermal method. Their structure and morphology were characterized by X-ray diffraction and scanning electron microscopy. The hybrid systems were used to fabricate direct conversion X-ray detectors able to operate with zero bias voltage. The detector performance was tested in a wide energy range using monochromatic synchrotron radiation. The addition of nanoparticles with high-Z elements improved the detector response to X-ray radiation compared with that of a pure organic P3HT:PCBM bulk heterojunction cell. The high dynamic range of our detector allows for recording X-ray absorption spectra, including the fine X-ray absorption structure located beyond the absorption edge. The obtained results suggest that nanocrystalline tungstates are promising candidates for application in direct organic–inorganic X-ray detectors.

Keywords: tungstates; hybrid organic–inorganic X-ray detectors; X-ray sensing

1. Introduction

Nowadays, developing new radiation detectors based on nanomaterials is an active field of research [1]. Among the different types of detectors, hybrid organic–inorganic systems for X-ray detection have attracted considerable attention during the last ten years [2]. The strong advantages of such systems are the combination of relatively inexpensive, easy-to-manufacture, flexible, and low-bias voltage (<10 V) organic semiconductors with high-Z inorganic (nano-)compounds [1,3–5]. The latter provide a large X-ray cross-section and control of spectral selectivity, which improve the absorption efficiency and sensitivity while maintaining the beneficial physical properties of the host organic matrix [2]. Various inorganic materials have been proposed for use in hybrid organic–inorganic systems for X-ray detection [2]. However, the search for the best system(s) that can be used in everyday applications remains one of the most important and challenging tasks in the field [6,7].

Here, we propose tungstates with a general chemical formula of AWO$_4$ [8] (where A is a divalent ion, for example, Ca, Sr, Ba, Pb, Ni, Zn, or Cd) as a new class of materials for use in hybrid organic–inorganic systems for direct-conversion X-ray detection. Using tungstates opens up a wide range of possibilities for solving a specific problem by optimizing their chemical composition and degree of crystallinity. This is convenient for producing hybrid systems but has not been exploited until now. Another advantage of tungstates for use in X-ray detectors is the high Z of tungsten (Z = 74) and the possibility of selecting the Z number of the second metal ion in a wide range. This allows for optimizing the absorption efficiency in a certain range of X-ray energies.

In this study, two possible candidates for use as the X-ray absorber in hybrid organic–inorganic direct X-ray detectors, i.e., nanocrystalline tungstates $CaWO_4$ and $ZnWO_4$ with the scheelite and wolframite crystallographic structures [8], respectively, were synthesized and characterized by X-ray diffraction (XRD) and scanning electron microscopy (SEM). The X-ray detectors were fabricated based on a mixture of nanotungstates with a P3HT:PCBM blend, and their ability to detect X-rays was demonstrated using tunable synchrotron radiation.

2. Materials and Methods

2.1. Nanoparticle Synthesis and Characterization

$CaWO_4$ and $ZnWO_4$ nanoparticles (NPs) were produced by the hydrothermal method [9]. Citric acid $C_6H_8O_7$ was used as a surfactant/capping agent and provided kinetic grain size control [10].

First, 3 mmol of $CaCl_2$ (97%, Alfa Aesar, Haverhill, MA, USA) and $Na_2WO_4 \cdot 2H_2O$ ($\geq$99%, 97%, Alfa Aesar, Haverhill, MA, USA) were separately dissolved in deionized water (Figure 1). Next, citric acid (1.5 mmol) was added to the $CaCl_2$ solution, and the obtained mixed solution was subsequently added to the $Na_2WO_4 \cdot 2H_2O$ solution. The solution pH was adjusted to 9 by adding an appropriate amount of NaOH ($\geq$98%, Sigma-Aldrich, St. Louis, MO, USA) solution in water. The obtained solution was mixed under constant magnetic stirring for 30 min. One part (16 mL) of the resulting solution was sealed in a Teflon-lined stainless-steel autoclave (25 mL) and was allowed to react at ~160 °C for 24 h, followed by natural cooling to room temperature. The rest of the solution was left at room temperature (RT) for 24 h for a comparison.
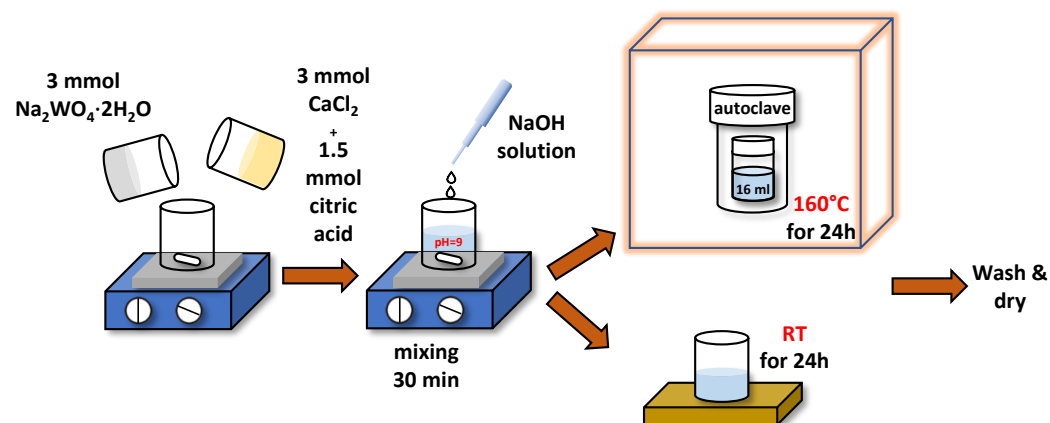

Figure 1. Schematics of $CaWO_4$ nanoparticle synthesis. See text for details.

The synthesis of $ZnWO_4$ NPs was analogous, only we used $Zn(NO_3)_2 \cdot 6H_2O$ (98%, Sigma-Aldrich, St. Louis, MO, USA) as the zinc source. Note that in this case, a lower pH value (pH = 8) was used, because an increase in pH to 9 resulted in ZnO impurities. The precipitates of nanotungstates obtained after hydrothermal treatment were washed and centrifuged several times in the following sequence: distilled water, isopropanol, acetone, and chlorobenzene, and finally dried in air at 75 °C.

The phase composition and crystallinity of all samples were controlled by powder X-ray diffraction (XRD) at room temperature using a benchtop Rigaku MiniFlex 600 diffractometer (Rigaku, Tokyo, Japan) with Bragg–Brentano geometry (Cu K_α radiation), operated at 40 kV and 15 mA. The crystallite size of NPs was estimated using the Rietveld refinement method as implemented in Profex software [11].

The sample morphology was studied by scanning electron microscopy (SEM) in immersion mode using a Helios 5 UX microscope (Thermo Fisher Scientific, Waltham, MA, USA) (Elstar in-lens SE TLD detector) operated at 2.00 kV. The particle-size distribution was evaluated considering the statistics of 200 NP measurements in the SEM micrographs.

2.2. Hybrid Organic–Inorganic X-ray Detector Fabrication and Measurements

Hybrid organic–inorganic X-ray detectors were fabricated on top of the 25×25 mm ITO (In_2O_3:Sn)-coated glass with a sheet resistance of 5 Ω/sq (Präzisions Glas & Optik GmbH). A poly(3,4-ethylenedioxythiophene)-poly(styrenesulfonate) (PEDOT:PSS; Heraeus Al4083) layer with a thickness of 40 nm was used as the hole transport and electron blocking layer. It was spin-coated in air (2500 rpm for 40 s with an acceleration of 2500 rpm/s) and annealed at 150 °C for 10 min.

A suspension of tungstate NPs and P3HT:PCBM was prepared by mixing the tungstate powder with a solution of the P3HT:PCBM mixture (weight ratio 1:1) in chlorobenzene (99.8% anhydrous, Sigma-Aldrich, St. Louis, MI, USA), followed by sonication of the premix for 1 h. The weight ratio of NPs:P3HT:PCBM in the suspension was 2:1:1. Thin films were fabricated from the suspension by the blade-casting method on a substrate heated to 75 °C. The P3HT:PCBM mixture was crystallized by annealing at 140 °C for 15 min.

We deposited a 5 nm thick hole-blocking layer of 4,7-diphenyl-1,10-phenanthroline (BPhen, Sigma-Aldrich, St. Louis, MI, USA) and 100 nm thick Al electrode on top of the hybrid layer by thermal evaporation in a vacuum at a pressure of less than 7×10^{-6} mbar. Al electrodes were deposited in a way that six separate "active pixels" with a size of 4×4 mm were formed and could be independently tested. Thus, the final hybrid organic–inorganic X-ray detector was composed of five ITO/PEDOT:PSS/NPs:P3HT:PCBM/BPhen /Al layers. The detectors were additionally encapsulated with glass to reduce their possible degradation in air. No significant degradation of the detectors was observed during the experiments.

X-ray measurements were conducted with the DESY PETRA-III P64 Advanced X-ray Absorption Spectroscopy undulator beamline [12]. The PETRA-III storage ring operated at $E = 6$ GeV and current $I = 100$ mA in top-up 40 bunch mode. Fixed-exit double-crystal monochromator Si (111) was used to select the required X-ray energy from the undulator photon source. The X-ray intensity I_0 before the sample was monitored with an ionization chamber. The beam size on the sample was about 1×1 mm. The hybrid organic–inorganic X-ray detector was placed inside the vacuum chamber and connected to a Keithley 428 current amplifier. The signal $I_{detector}$ was measured with the P64 beamline ionization chamber monitoring setup. The absolute values of the detected photocurrent were in the range of 0.1–1.0 nA. A passivated implanted planar silicon (PIPS) detector (Canberra) was used for the simultaneous detection of X-ray fluorescence. All measurements were recorded in a dark environment to exclude possible photoelectric effects induced by light in the experimental hutch.

3. Results and Discussion

Bulk $CaWO_4$ and $ZnWO_4$ tungstates have different crystallographic structures (scheelite and wolframite [8]) composed of WO_4 tetrahedral and WO_6 octahedral units (see the insets in Figure 2), respectively. Both calcium and zinc ions are coordinated with oxygen ions; however, calcium ions have eight-fold coordination, while zinc ions have six-fold coordination. In scheelite $CaWO_4$, Ca^{2+} cations are located between slightly distorted WO_4 tetrahedra [13], whereas in wolframite $ZnWO_4$, distorted WO_6 and ZnO_6 octahedra are connected by edges and form infinite zigzag chains [14]. Both tungstates can be prepared in the nanocrystalline form [15,16].
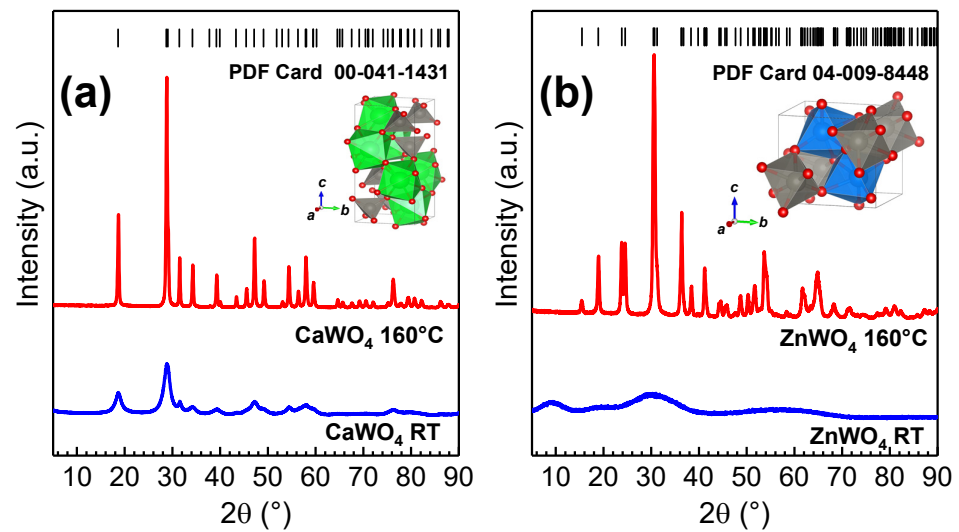
Figure 2. X-ray diffraction patterns of CaWO$_4$ (**a**) and ZnWO$_4$ (**b**) nanoparticles left at RT (**bottom**) and treated at ∼160 °C for 24 h (**middle**). The standard PDF cards of the CaWO$_4$ (PDF Card 00-041-1431) and ZnWO$_4$ (PDF Card 04-009-8448) phases are shown for comparison at the (**top**). The crystal structures of the tungstates are shown in the insets.

The XRD patterns of CaWO$_4$ and ZnWO$_4$ nanocrystalline samples synthesized at RT and using hydrothermal treatment at ∼160 °C for 24 h in the autoclave are shown in Figure 2. The CaWO$_4$ nanoparticles prepared at RT demonstrated weak crystallinity, while the ZnWO$_4$ nanoparticles were amorphous. At the same time, the XRD patterns of hydrothermally treated tungstate samples contained many Bragg peaks, which could be indexed to the pure tungstate phases (PDF Card 00-041-1431 for CaWO$_4$ and PDF Card 04-009-8448 for ZnWO$_4$): tetragonal phase (space group $I4_1/a$) with the lattice constants $a = b = 5.246$ Å and $c = 11.380$ Å for CaWO$_4$ and monoclinic phase (space group $P2/c$) with the lattice constants $a = 4.690$ Å, $b = 5.734$ Å and $c = 4.940$ Å for ZnWO$_4$. The average crystallite sizes of hydrothermally grown CaWO$_4$ and ZnWO$_4$ nanotungstates were determined using Rietveld refinement and were equal to ∼43 nm and ∼30 nm, respectively. The CaWO$_4$ seeds for nanoparticle synthesis left at RT for 24 h had a size of ∼5 nm.

Both tungstates have different morphology, as shown in the SEM micrographs (Figure 3). Products synthesized at RT formed fine powders with agglomerated particles (Figure 3a,b). The crystallinity was significantly improved after hydrothermal treatment at ∼160 °C as evidenced by the well-defined facets of the particles (Figure 3c,d). CaWO$_4$ formed microspheres composed of irregular polyhedral NPs having an approximate average diameter of 45 nm with a standard deviation of 10 nm (Figure 3c). This estimate is in agreement with the average crystallite size found from the XRD data. For ZnWO$_4$, rod-like morphology and higher uniformity were evident (Figure 3d). Individual ZnWO$_4$ nanorods with a length of 62 ± 14 nm and a diameter of 25 ± 3 nm were resolved. The average crystallite size estimated by XRD was between the determined length and diameter values of particles from the SEM micrographs.
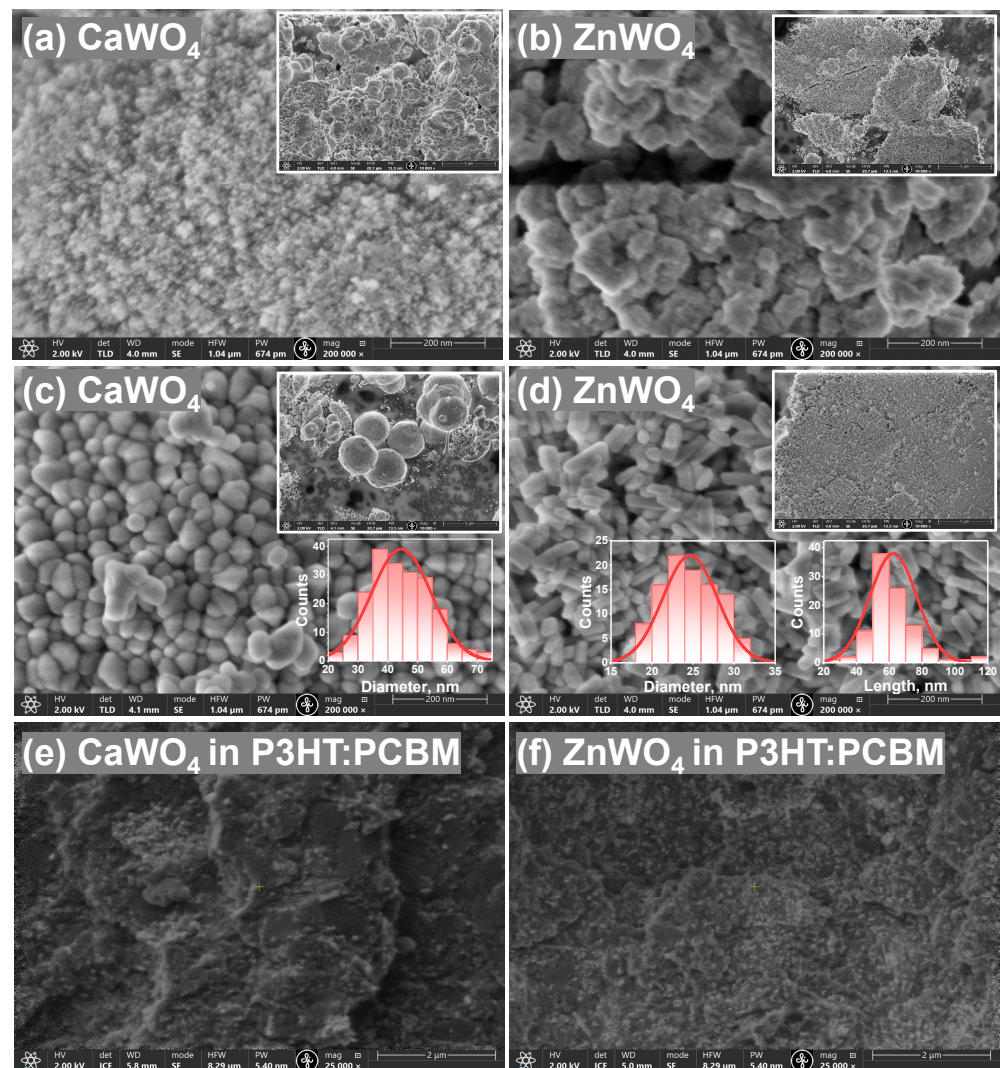
Figure 3. SEM micrographs of CaWO$_4$ and ZnWO$_4$ nanoparticles at RT (**a**,**b**) and treated at ~160 °C for 24 h (**c**,**d**). Cross-section SEM images of fabricated hybrid detectors (part of tungstate NPs incorporated in a P3HT:PCBM matrix) are also shown in (**e**,**f**). The particle-size distributions of CaWO$_4$ (diameter of nanoparticles) and ZnWO$_4$ (diameter and length of nanorods) estimated from the corresponding SEM micrographs are shown in the insets in (**c**,**d**), respectively.

Hydrothermally treated tungstate NPs were incorporated into a P3HT:PCBM matrix to fabricate a hybrid organic–inorganic direct-conversion X-ray detector. The concentration of the NPs:P3HT:PCBM suspension used for the active layer deposition in this study was fixed at a weight ratio of 2:1:1. It can be seen in the cross-sectional SEM images (Figure 3e,f) that after mixing, the NPs distributed fairly uniformly in the hybrid layer. The thickness of the active layer with CaWO$_4$:P3HT:PCBM (ZnWO$_4$:P3HT:PCBM) was ~17 μm (~16 μm).

The X-ray detectors were fabricated with a sandwich-type architecture and multilayer stacking as depicted in Figure 4a. The detectors were realized on the top of the ITO-coated glass substrate. A polymer mixture of two ionomers PEDOT:PSS was used as the hole transport and electron blocking layer. The active layer was composed of a NPs:P3HT:PCBM mixture. Bathophenanthroline (BPhen) played the role of a hole-blocking layer on top of the active layer due to its wide energy gap and high ionization potential [17,18]. Finally, aluminium film was used as a top electrode, and the whole structure was encapsulated under a glass. A detector without NPs (pure P3HT:PCBM ~3.3 μm thick layer) was also fabricated for comparison. The experiment scheme and a photo of one of the detectors are shown in Figure 4b.
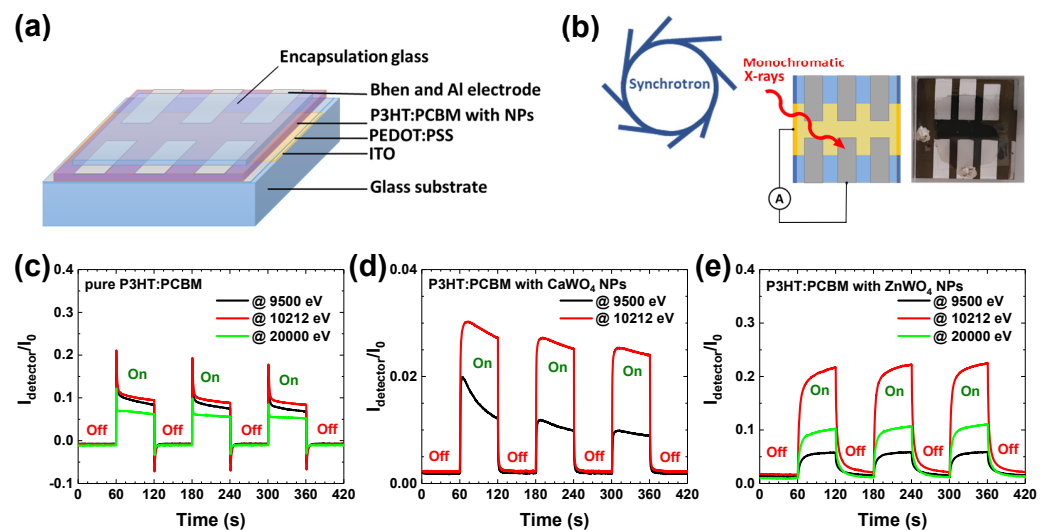
Figure 4. A schematic representation of fabricated hybrid organic–inorganic direct-conversion X-ray detectors (**a**). A scheme of X-ray response measurements at synchrotron, and a photo of fabricated X-ray detector (**b**). X-ray−induced response signals ($I_{detector}/I_0$) for pure P3HT:PCBM (**c**), hybrid CaWO$_4$+P3HT:PCBM (**d**), and ZnWO$_4$+P3HT:PCBM (**e**) systems under repeated X-ray exposures (on/off cycles).

The P3HT:PCBM blend is one of the most studied and used active materials for bulk heterojunction organic solar cells [19], which show good efficiency in the visible and UV ranges. In the X-ray range, the absorption probability strongly depends on the atomic number Z, the density of the material, and the incident X-ray photon energy. Therefore, organic polymers exhibit a low X-ray attenuation coefficient (especially in the hard X-ray range) that can be improved by the incorporation of inorganic particles including elements with a high atomic number (high-Z) values [2].

Note that a sharp rise in the X-ray absorption coefficient, called the X-ray absorption edge, is observed for elements at particular X-ray energies when the incident X-ray energy is equal to that of the binding energy of a core-level electron. For instance, Ca ($Z = 20$) and Zn ($Z = 30$) have K edges at 4038.5 eV and 9659 eV, respectively, whereas the more heavy W ($Z = 74$) has L$_3$-edge at 10,207 eV [20]. A strong increase in absorption beyond the edge can be used for the optimization of detector spectral sensitivity in a required energy range. In some compounds, intense absorption, the so-called "white line" (WL), is observed just above the edge. Its existence is common in X-ray absorption spectra of tungsten oxide compounds at the W L$_{2,3}$ edges and is caused by quasilocalized 5d(W) states [21,22]. In this study, we employed the presence of the WL, located at 10,212 eV at the W L$_3$ edge, to amplify the signal of detectors containing tungstates.

The fabricated hybrid detectors were exposed to monochromatic synchrotron radiation at three selected X-ray photon energies (9500 eV, 10,212 eV, and 20,000 eV) to study the effects of tungstate NPs present in the active layer on the detector response. The first energy value (9500 eV) was selected between the K edges of Ca and Zn, the second energy value (10,212 eV) was located at the WL maximum of the tungsten L$_3$ edge, and the third energy value (20,000 eV) was chosen well above all absorption edges in the two tungstates.

When X-ray photons are absorbed in matter, electron–hole pairs are generated via the internal photoelectric effect, followed by an avalanche of secondary generated electrons. In the detector, the charge carriers are transported to the electrodes and can be detected as electric current. Note that similar to polymer solar cells [23], our hybrid P3HT:PCBM-based detectors can operate without any external bias voltage.

Time-dependent X-ray experiments for three detectors were performed at the above-mentioned incident X-ray energies by periodically turning the incident X-rays on and off with a 120 s period. Note that only two X-ray energies (9500 eV and 10,212 eV) were used in the case of the CaWO$_4$-based detector. The normalized X-ray response on/off signals,

i.e., the intensity ratio $I_{detector}(E)/I_0(E)$, where $I_0(E)$ corresponds to the incident X-ray intensity measured by the ionization chamber, and $I_{detector}(E)$ is the signal detected by the detector, are shown in Figure 4c–e. As one can see, all three detectors demonstrated sensitivity to X-rays in a form close to a square-shaped response, which differs from the saw-tooth-shaped photocurrent response observed in some organic [5] and hybrid [24] X-ray detectors. Note the different *y*-axis scale in Figure 4d. It is difficult to compare absolute values of the photocurrent for different detectors because they are strongly affected by the fabrication quality. Nevertheless, we can compare relative responses at different energies.

A response to exposure to X-rays of the pure organic P3HT:PCBM detector is shown in Figure 4c. Because organic polymers are composed of light elements, they exhibit a low X-ray attenuation coefficient and are less sensitive at larger energies. As a result, the photogenerated current is close for X-ray photons at 9500 eV and 10,212 eV but is smaller at 20,000 eV. After X-ray illumination begins, the top of the current pulse relaxes and drops by about 30–50% during the first seconds. When the shutter blocs the X-rays, the dark current becomes slightly negative and relaxes back to the initial value. The sharp signal at the X-ray shutter switching points is presumably related to the charge trapping/detrapping at material/electrode interfaces and space charge effects [25,26].

The X-ray-induced response of both hybrid detectors with nanoparticles (Figure 4d,e) was close after sufficient stabilization time and is similar to that found in other hybrid detectors [27,28]. The presence of tungstate nanoparticles significantly (3–4 times) enhanced the response of the detector at the energy of 10,212 eV just above the W L_3 edge due to the presence of the strong absorption resonance ("white line") [21,22]. In the case of the $ZnWO_4$-based detector (Figure 4e), an additional contribution came from the absorption caused by the Zn K-edge located at 9659 eV. Note that the X-ray absorption caused by tungsten $L_{1,2,3}$ edges, located at 10,207 eV, 11,544 eV, and 12,100 eV, respectively, contributed as much as up to 20,000 eV. As a result, the response of the $ZnWO_4$-based detector was about two times larger at 20,000 eV than at 9500 eV.

Finally, we used a hybrid detector with $ZnWO_4$ nanoparticles to record the Ni K-edge X-ray absorption spectrum of a Ni foil (Figure 5). A PIPS detector was simultaneously used in fluorescence mode for comparison. As one can see, the X-ray absorption near-edge structure (XANES) $\mu(E)$ measured in continuous scan mode by the hybrid detector exhibited broadened oscillations; nevertheless, all main spectral features were present. The observed broadening was caused by the slow response of the hybrid detector compared with PIPS. The broadening effect decreased in the range of the extended X-ray absorption fine structure (EXAFS) $\chi(k)k^2$ ($k = \sqrt{(2m_e/\hbar^2)(E - E_0)}$, where m_e is the electron mass, $\hbar$ is the Planck constant, and E_0 is the threshold energy, i.e., the energy of a free electron with zero momentum), located beyond the absorption edge, due to the frequency of oscillations of the absorption coefficient becoming gradually lower with increasing energy [29]. Note the good agreement between the EXAFS spectra measured by the two detectors at large wave numbers k, where the signal is multiplied by the k^2 factor. This finding suggests a good dynamic range of the $ZnWO_4$-based hybrid detector.
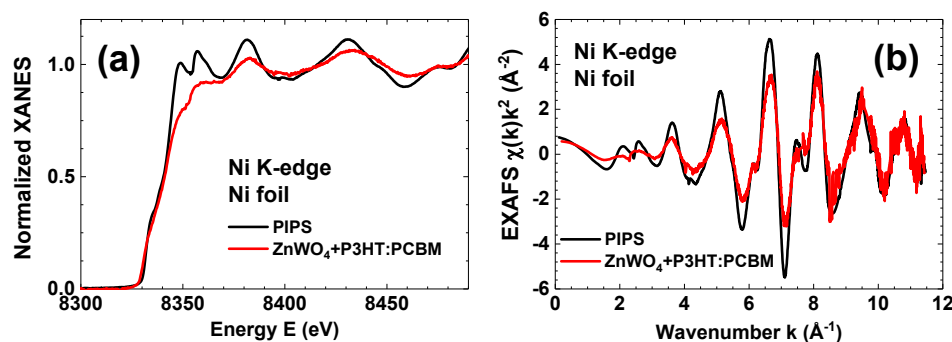

Figure 5. Comparison of the Ni K-edge (**a**) XANES $\mu(E)$ and (**b**) EXAFS spectra $\chi(k)k^2$ of nickel foil measured using novel hybrid and PIPS detectors. *k* is the wavenumber of the excited photoelectron.

4. Conclusions

Nanocrystalline $CaWO_4$ and $ZnWO_4$ tungstates were studied as promising candidates for use in hybrid organic–inorganic direct-conversion X-ray detectors operating without a bias voltage. The tungstate nanoparticles (NPs) with a crystallite size of ∼43 nm for $CaWO_4$ and ∼30 nm for $ZnWO_4$ were synthesized by the hydrothermal method with different morphologies.

Hybrid organic–inorganic X-ray detectors were fabricated on top of ITO-covered glass and had a sandwich-type structure composed of five ITO/PEDOT:PSS/NPs:P3HT:PCBM/BPhen/Al layers. A pure organic detector without nanoparticles was used for comparison. Feasibility experiments were performed using monochromatic synchrotron radiation allowing us to conduct the measurements in a wide X-ray energy range (9000–20,000 eV). We showed that the presence of tungstate nanoparticles with high-Z elements increases the X-ray attenuation efficiency and, thus, improves the response of the hybrid detector to X-rays compared with those of a pure organic one based on a P3HT:PCBM bulk heterojunction cell. The use of the developed detector for spectroscopic applications was also demonstrated by recording the Ni K-edge X-ray absorption spectrum of nickel foil. Its well-resolved and extended fine X-ray absorption structure indicates the high dynamic range of the detector.

Such hybrid detectors with different AWO_4 tungstate nanoparticles can provide a cost-effective solution that can be optimized for a particular energy range by selecting the A-cation type and operating without external voltage.

Abbreviations

The following abbreviations are used in this manuscript:

EXAFS	Extended X-ray absorption fine structure
NP	nNanoparticle
PEDOT:PSS	Poly(3,4-ethylenedioxythiophene)-poly(styrenesulfonate)
P3HT:PCBM	Poly(3-hexylthiophene-2,5-diyl):Phenyl-C61-butyric acid methyl ester
RT	Room temperature
SEM	Scanning electron microscopy
WL	White line
XANES	X-ray absorption near edge structure
XRD	X-ray diffraction

References

1. Luo, Z.; Moch, J.G.; Johnson, S.S.; Chen, C.C. A review on X-ray detection using nanomaterials. *Curr. Nanosci.* **2017**, *13*, 364–372. [CrossRef]

2. Thirimanne, H.; Jayawardena, K.D.G.I.; Parnell, A.J.; Bandara, R.M.I.; Karalasingam, A.; Pani, S.; Huerdler, J.E.; Lidzey, D.G.; Tedde, S.F.; Nisbet, A.; et al. High sensitivity organic–inorganic hybrid X-ray detectors with direct transduction and broadband response. *Nat. Commun.* **2018**, *9*, 2926. [CrossRef]

3. Fraboni, B.; Ciavatti, A.; Merlo, F.; Pasquini, L.; Cavallini, A.; Quaranta, A.; Bonfiglio, A.; Fraleoni-Morgera, A. Organic semiconducting single crystals as next generation of low-cost, room-temperature electrical X-ray detectors. *Adv. Mater.* **2012**, *24*, 2289–2293. [CrossRef] [PubMed]

4. Suzuki, T.; Miyata, H.; Katsumata, M.; Nakano, S.; Matsuda, K.; Tamura, M. Organic semiconductors as real-time radiation detectors. *Nucl. Instrum. Methods A* **2014**, *763*, 304–307. [CrossRef]

5. Basirico, L.; Ciavatti, A.; Cramer, T.; Cosseddu, P.; Bonfiglio, A.; Fraboni, B. Direct X-ray photoconversion in flexible organic thin film devices operated below 1V. *Nat. Commun.* **2016**, *7*, 13063. [CrossRef]

6. Liu, J. Flexible, printable soft-X-ray detectors based on all-inorganic perovskite quantum dots. *Adv. Mater.* **2019**, *31*, 1901644. [CrossRef]

7. Mescher, H.; Schackmar, F.; Eggers, H.; Abzieher, T.; Zuber, M.; Hamann, E.; Baumbach, T.; Richards, B.S.; Hernandez-Sosa, G.; Paetzold, U.W.; et al. Flexible inkjet-printed triple cation perovskite X-ray detectors. *ACS Appl. Mater. Interfaces* **2020**, *12*, 15774. [CrossRef]

8. Sleight, A.W. Accurate cell dimensions for ABO_4 molybdates and tungstates. *Acta Cryst. B* **1972**, *28*, 2899–2902. [CrossRef]

9. Lee, J.; Rancilio, N.J.; Poulson, J.M.; Won, Y.Y. Block copolymer-encapsulated $CaWO_4$ nanoparticles: Synthesis, formulation, and characterization. *ACS Appl. Mater. Interfaces* **2016**, *8*, 8608–8619. [CrossRef]

10. Su, Y.; Li, G.; Xue, Y.; Li, L. Tunable physical properties of $CaWO_4$ nanocrystals via particle size control. *J. Phys. Chem. C* **2007**, *111*, 6684–6689. [CrossRef]

11. Doebelin, N.; Kleeberg, R. Profex: A graphical user interface for the Rietveld refinement program BGMN. *J. Appl. Crystallogr.* **2015**, *48*, 1573–1580. [CrossRef] [PubMed]

12. Caliebe, W.A.; Murzin, V.; Kalinko, A.; Gorlitz, M. High-flux XAFS-beamline P64 at PETRA III. *AIP Conf. Proc.* **2019**, *2054*, 060031. [CrossRef]

13. Gürmen, E.; Daniels, E.; King, J.S. Crystal structure refinement of $SrMoO_4$, $SrWO_4$, $CaMoO_4$, and $BaWO_4$ by neutron diffraction. *J. Chem. Phys.* **1971**, *55*, 1093–1097. [CrossRef]

14. Schofield, P.F.; Knight, K.S.; Cressey, G. Neutron powder diffraction study of the scintillator material. *J. Mater. Sci. A* **1996**, *31*, 2873. [CrossRef]

15. Liu, S.; Tian, S.; Xing, R. $CaWO_4$ hierarchical nanostructures: Hydrothermal synthesis, growth mechanism and photoluminescence properties. *CrystEngComm* **2011**, *13*, 7258–7261. [CrossRef]

16. Pereira, P.F.S.; Gouveia, A.F.; Assis, M.; de Oliveira, R.C.; Pinatti, I.M.; Penha, M.; Goncalves, R.F.; Gracia, L.; Andres, J.; Longo, E. $ZnWO_4$ nanocrystals: Synthesis, morphology, photoluminescence and photocatalytic properties. *Phys. Chem. Chem. Phys.* **2018**, *20*, 1923–1937. [CrossRef]

17. Chen, H.Y.; Lam, W.Y.; Luo, J.D.; Ho, Y.L.; Tang, B.Z.; Zhu, D.B.; Wong, M.; Kwok, H.S. Highly efficient organic light-emitting diodes with a silole-based compound. *Appl. Phys. Lett.* **2002**, *81*, 574–576. [CrossRef]

18. Ma, Z.; Zhao, J.; Wang, X.; Yu, J. Effect of bulk and planar heterojunctions based charge generation layers on the performance of tandem organic light-emitting diodes. *Org. Electron.* **2016**, *30*, 136–142. [CrossRef]

19. Ameri, T.; Khoram, P.; Min, J.; Brabec, C.J. Organic ternary solar cells: A review. *Adv. Mater.* **2013**, *25*, 4245–4266. [CrossRef]

20. *X-ray Data Booklet*, 3rd ed.; Lawrence Berkeley National Laboratory, University of California: Davis, CA, USA, 2009.

21. Balerna, A.; Bernieri, E.; Burattini, E.; Kuzmin, A.; Lusis, A.; Purans, J.; Cikmach, P. XANES studies of MeO_{3-x} (Me = W, Re, Ir) crystalline and amorphous oxides. *Nucl. Instrum. Methods Phys. Res. A* **1991**, *308*, 240–242. [CrossRef]

22. Kalinko, A.; Kuzmin, A. Static and dynamic structure of $ZnWO_4$ nanoparticles. *J. Non-Cryst. Solids* **2011**, *357*, 2595–2599. [CrossRef]

23. Cai, W.; Gong, X.; Cao, Y. Polymer solar cells: Recent development and possible routes for improvement in the performance. *Sol. Energy Mater. Sol. Cells* **2010**, *94*, 114–127. [CrossRef]

24. Jayawardena, K.D.G.I.; Thirimanne, H.M.; Tedde, S.F.; Huerdler, J.E.; Parnell, A.J.; Bandara, R.M.I.; Mills, C.A.; Silva, S.R.P. Millimeter-scale unipolar transport in high sensitivity organic–inorganic semiconductor X-ray detectors. *ACS Nano* **2019**, *13*, 6973–6981. [CrossRef]

25. Haneef, H.F.; Zeidell, A.M.; Jurchescu, O.D. Charge carrier traps in organic semiconductors: A review on the underlying physics and impact on electronic devices. *J. Mater. Chem. C* **2020**, *8*, 759–787. [CrossRef]

26. Butanovs, E.; Zolotarjovs, A.; Kuzmin, A.; Polyakov, B. Nanoscale X-ray detectors based on individual CdS, SnO_2 and ZnO nanowires. *Nucl. Instrum. Methods Phys. Res. A* **2021**, *1014*, 165736. [CrossRef]

27. Nanayakkara, M.P.A.; Matjacic, L.; Wood, S.; Richheimer, F.; Castro, F.A.; Jenatsch, S.; Zufle, S.; Kilbride, R.; Parnell, A.J.; Masteghin, M.G.; et al. Ultra-low dark current organic–inorganic hybrid X-ray detectors. *Adv. Funct. Mater.* **2020**, *31*, 2008482. [CrossRef]

28. Xiang, L.; Huang, X.; Wang, Y.; Xin, Z.; Chai, G.; Xu, Y.; Wang, K.; Chen, J.; Liu, C.; Wang, X.; et al. X-ray Sensitive hybrid organic photodetectors with embedded CsPbBr$_3$ perovskite quantum dots. *Org. Electron.* **2021**, *98*, 106306. [CrossRef]
29. Rehr, J.J.; Albers, R.C. Theoretical approaches to X-ray absorption fine structure. *Rev. Mod. Phys.* **2000**, *72*, 621–654. [CrossRef]